Jets from shocked metal surfaces with grooves: Missing experiments

Kaiser, Bryan Edward
Tregillis, Ian Lee
Cherne, Frank Joseph
Koskelo, Aaron C.

To be published in: Journal of Applied Physics

DOI to publisher's version: 10.1063/5.0203810

Journal of Applied Physics

PERSPECTIVE | MAY 02 2024

Jets from shocked metal surfaces with grooves: Missing experiments

B. E. Kaiser ; I. L. Tregillis ; F. J. Cherne ; A. C. Koskelo

J. Appl. Phys. 135, 170903 (2024)
https://doi.org/10.1063/5.0203810

Journal of Applied Physics PERSPECTIVE pubs.aip.org/aip/jap

Jets from shocked metal surfaces with grooves: Missing experiments

Cite as: J. Appl. Phys. **135**, 170903 (2024); doi: 10.1063/5.0203810
Submitted: 16 February 2024 · Accepted: 15 April 2024 ·
Published Online: 2 May 2024

B. E. Kaiser,[1,a)] I. L. Tregillis,[2] F. J. Cherne,[3] and A. C. Koskelo[1]

AFFILIATIONS

[1]Verification and Analysis, Los Alamos National Laboratory, Los Alamos, New Mexico 87545, USA
[2]Plasma Theory and Applications, Los Alamos National Laboratory, Los Alamos, New Mexico 87545, USA
[3]Shock and Detonation Physics, Los Alamos National Laboratory, Los Alamos, New Mexico 87545, USA

[a)]**Author to whom correspondence should be addressed:** bkaiser@lanl.gov

ABSTRACT

Many studies have investigated the mass outflows generated when a planar shock transits an imperfect ("defected") metal surface, where the defects are symmetric triangular or sinusoidal grooves. Yet a fundamental question remains unanswered: how does the quantity of outflow mass and its maximum velocity vary as a function of the groove cross-sectional aspect ratio? We identify two sets of missing experiments that must be addressed to answer the question. The aspect ratio (groove depth over width) is equivalently represented by θ, the cross-sectional half angle, or by $\eta_0 k$, the amplitude multiplied by an effective wavenumber. Low θ (high $\eta_0 k$) grooves comprise the first set of missing experiments, which are necessary to determine the validity of theoretical predictions of the nonlinear regime ($\eta_0 k \geq 1$, $\theta < 57.5°$). The second set of missing experiments are those in which the volume of the groove (or equivalently, the axial cross-sectional area) has been held constant as θ or $\eta_0 k$ are varied. Such experiments are necessary to *independently* measure the effects of variations in groove volume and groove aspect ratio on the resulting jets.

I. INTRODUCTION

The dynamics of imperfect ("defected") shocked metal surfaces are applicable to industrial and military applications.[1] In this *Perspective*, we aggregate previously reported experimental data and identify two sets of missing experiments. Our inquiry is limited to metal surfaces with groove defects subjected to sufficiently strong shock pressures such that the metal changes partially or completely to fluid phase by shock breakout. In the case of shocked defects, and Richtmyer–Meshkov Instabilities[2–4] (RMI) in general, baroclincity is generated at a perturbed interface as the shock transits. RMI is the physical process by which shock-induced baroclincity causes vorticity deposition and subsequent motion at interfaces, whereas RMI theory refers to an idealized modal model initially proposed by Richtmyer[2] for small-amplitude interface perturbations. Baroclinicity generates momentum curl (i.e., non-zero vorticity $\boldsymbol{\omega} = \nabla \times \mathbf{u} \neq 0$) in fluids.[4] In the case of symmetric concave interface perturbations, (i.e., grooves), baroclinic momentum curl produces mass convergence along the centerline of the groove. If the fluid is approximately incompressible, then mass conservation requires material to be ejected (jetted) from the surface in the positive x direction in Fig. 1.

Accelerations from heavy-to-light material in metal–void or metal–gas interfaces are a limiting case of RMI where the Atwood number,

$$\mathrm{At} = \frac{\rho_{\mathrm{void}} - \rho_{\mathrm{metal}}}{\rho_{\mathrm{void}} + \rho_{\mathrm{metal}}}, \tag{1}$$

approaches -1, where ρ_{metal} is the density of solid, pre-shock, metal and ρ_{void} is significantly less dense than solid metal such that $\rho_{\mathrm{void}} \ll \rho_{\mathrm{metal}}$. Fluid jets or spikes seeded by grooves on shocked metal–void interfaces are a source of the particulate sprays commonly referred to as ejecta.[5] Here, we examine ejecta produced by jetting from symmetric triangular and sinusoidal grooves along metal–void or metal–gas interfaces characterized by At ≈ -1.

Figure 1 depicts all relevant geometric information. We assume that groove length, L_z, is much longer than the groove

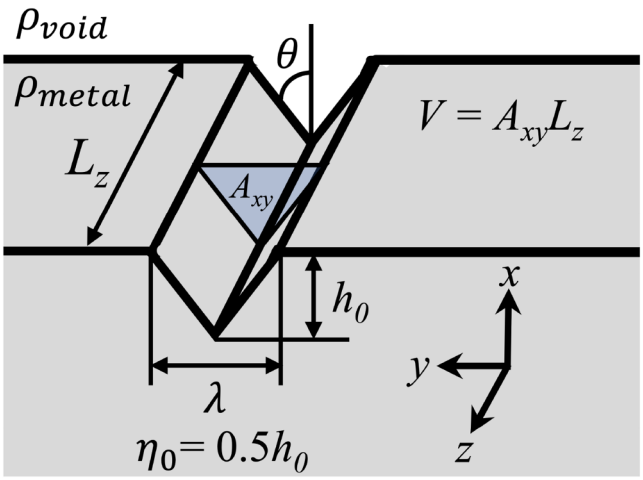

FIG. 1. Groove defect geometry. The free surface normal direction is the positive x direction. The planar shock transits the free surface and moves in the positive x direction from below (negative x). All of the geometric relations displayed here also applied to sinusoidal defects. Above the free surface is a void that is either a vacuum or filled with low density gas such that At ≈ -1.

width, λ,

$$\frac{\lambda}{L_z} \ll 1, \tag{2}$$

and much longer than the groove depth $h_0 = 2\eta_0$,

$$\frac{h_0}{L_z} \ll 1. \tag{3}$$

The axial groove aspect ratio is defined as

$$\alpha = \frac{h_0}{\lambda}, \tag{4}$$

and it is commonly represented by two interchangeable variables, the axial amplitude-wavenumber product $\eta_0 k$ and the groove half-angle θ, where η_0 is the amplitude and $k = 2\pi/\lambda$ is the effective wavenumber of the groove.[6] The half angle is calculated as

$$\tan\theta = \frac{1}{2\alpha}, \tag{5}$$

where $\eta_0 k$ and θ are connected through the relationship,

$$\eta_0 k = \frac{\pi}{2\tan\theta}. \tag{6}$$

Groove volume is given by

$$V = A_{xy}L_z, \tag{7}$$

where A_{xy} is the axial cross-sectional area. For symmetric triangular or sinusoidal grooves,

$$A_{xy,\mathrm{tri}} = \eta_0\lambda, \tag{8}$$

$$A_{xy,\mathrm{sine}} = \frac{\eta_0\lambda}{\pi}, \tag{9}$$

respectively.

Despite nearly eight decades of investigation,[1] two fundamental questions lack answers supported by empirical evidence.

1. How does jetting behavior vary in the limit as $\alpha \gg 1$ (narrow, deep grooves) for symmetric triangular and sinusoidal grooves?
2. What is the effect of variable aspect ratio on jets from symmetric triangular and sinusoidal grooves?

It is understood that grooves with larger volumes produce more outflow mass,[7,8] both from continuum mechanical reasoning and from observations, assuming all other defect and shock properties are held constant. For example, recent experiments by Xin *et al.*[7] (shots 2 and 4) suggest that a symmetric triangular groove with a 215% larger cross-sectional area produces 152% more outflow mass for grooves with the same length L_z in Sn targets at approximately 25 GPa. If increasing groove volume is known to increase outflow mass, then *groove volume must be held constant* to independently assess the effect of groove aspect ratio variability on jet mass.

A. Salient non-dimensional variables

Non-dimensionalization aids experiment reproducibility and inter-experiment comparison.[9,10] Non-dimensionalization is particularly useful for the investigation of jets from shocked surface grooves because jets can occur over a broad range of length and time scales. The velocity ratio U is

$$U = \frac{u_\infty}{u_{fs}}, \tag{10}$$

where u_∞ is a characteristic velocity of the jet tip at late times and u_{fs} is the velocity of the planar free surface outside of the groove where the surface normal is exactly parallel to the direction of shock propagation. The jetting factor[8] is defined as

$$J = \frac{m}{\rho_0 V} = \frac{m}{m_0} \in [0, \infty). \tag{11}$$

The jetting factor was originally represented by $R(\theta)$;[8] we change the notation to avoid confusion with roughness parameters. $m_0 = \rho_0 V$ is the "missing mass" of the pre-shock groove, ρ_0 is the pre-shock density of the metal $[\rho_0 = \rho_{\mathrm{metal}}(t = 0)]$ in Fig. 1 [Eq. (1)], V is the defect volume [Eq. (7)], and m is the total quantity of metal mass that is ejected beyond the free surface position.

B. Salient dimensional variables

The groove volume V can be difficult to measure accurately and is only rarely reported in experimental studies, presumably because outflow mass is measured per unit area and may be assumed uniform over the length of the groove away from the groove ends.

However, information pertaining to groove axial cross-sectional area, A_{xy}, is regularly measured and reported. Measurements of jet mass, m, per unit area are referred to as areal mass,

$$\rho_A = \frac{m}{A_{\text{surf}}}, \tag{12}$$

where typically A_{surf} is a surface on which outflow mass accumulates that is anti-parallel to the free surface normal direction. We propose the adoption of the areal jetting factor per unit length,

$$J_A = \frac{\rho_A}{\rho_0 A_{xy}} \in [0, \infty), \tag{13}$$

because it contains commonly reported variables in groove experiments. It is interpretable as the amount of areal mass ejected per unit length for grooves that satisfy limiting conditions of Eqs. (2) and (3),

$$J_A \neq \frac{J}{L_z}, \tag{14}$$

unless $A_{\text{surf}} = L_z^2$, in which case, Eqs. (2) and (3) would not be satisfied. For all of the surveyed experiments here, $A_{\text{surf}} \neq L_z^2$. $J_A A_{xy}$ is equivalent to Asay and Bertholf's "normalized ejecta mass" length scale $\mathcal{M}$,[8]

$$\mathcal{M} = \frac{JV}{A_{\text{surf}}}, \tag{15}$$

$$= \frac{m}{\rho_0 A_{\text{surf}}}, \tag{16}$$

$$= J_A A_{xy}. \tag{17}$$

C. Boundary conditions imposed by groove geometry

The groove geometry depicted in Fig. 1 imposes certain boundary conditions on velocity ratio U and jetting factors J and J_A. For zero depth and/or infinitely wide grooves ($\alpha \to 0$), the velocity ratio must be unity (assuming that $|u_{fs}| > 0$) and the jet mass and cross-sectional area must vanish, therefore,

$$\lim_{\theta \to 90^\circ} U = \lim_{\eta_0 k \to 0} U = 1, \tag{18}$$

$$\lim_{\theta \to 90^\circ} m = \lim_{\eta_0 k \to 0} m = 0, \tag{19}$$

$$\lim_{\theta \to 90^\circ} A_{xy} = \lim_{\eta_0 k \to 0} A_{xy} = 0, \tag{20}$$

and, therefore, the groove volume [Eq. (7)] vanishes as well. However, jetting behavior as $\alpha \to 0$ is complicated by additional physics, such as viscous effects, that do not appreciably affect the dynamics at $\alpha > 0$. Moreover, machining tolerances and finite target geometries impose limits on experimental groove geometries. If the jet vanishes before the volume vanishes, presumably because the baroclinicity is too weak to induce material flow,

$$\lim_{\theta \to 90^\circ} \frac{m}{A_{xy}} = \lim_{\eta_0 k \to 0} \frac{m}{A_{xy}} = 0, \tag{21}$$

then

$$\lim_{\theta \to 90^\circ} J = \lim_{\eta_0 k \to 0} J = 0, \tag{22}$$

$$\lim_{\theta \to 90^\circ} J_A = \lim_{\eta_0 k \to 0} J_A = 0. \tag{23}$$

Similarly, for infinite depth and/or zero width grooves ($\alpha \to \infty$),

$$\lim_{\theta \to 0^\circ} U = \lim_{\eta_0 k \to \infty} U = 1, \tag{24}$$

$$\lim_{\theta \to 0^\circ} m = \lim_{\eta_0 k \to \infty} m = 0, \tag{25}$$

$$\lim_{\theta \to 0^\circ} A_{xy} = \lim_{\eta_0 k \to \infty} A_{xy} = 0, \tag{26}$$

and again the groove volume [Eq. (7)] vanishes as well. If we assume, perhaps due to frictional forces that suppress the jetting of very narrow and deep grooves, that

$$\lim_{\theta \to 0^\circ} \frac{m}{A_{xy}} = \lim_{\eta_0 k \to \infty} \frac{m}{A_{xy}} = 0, \tag{27}$$

then

$$\lim_{\theta \to 0^\circ} J = \lim_{\eta_0 k \to \infty} J = 0, \tag{28}$$

$$\lim_{\theta \to 0^\circ} J_A = \lim_{\eta_0 k \to \infty} J_A = 0. \tag{29}$$

These physically and geometrically derived limits are useful in the evaluation of theories and experiments.

II. SYNOPSIS OF SELECTED THEORIES

In this section, we briefly discuss the essential differences between two jet prediction theories and one empirically fitted model. The objective is to briefly describe the essential underlying assumptions and to identify those that are, and are not, common to the theories. The empirically fitted model is commonly known as "missing mass theory."[11,12] We refer to it as an empirically fitted model rather than a theory because it is a linear regression of empirical data observed by Asay and Bertholf[8] in their Fig. 9. The first theory is known variously as "steady jetting theory,"[13] "steady-state theory,"[14] or "steady-jet theory,"[15] and it is shaped charge liner jet theory,[16,17] originally formulated to predict jets from thin metal groove liners surrounded by high explosives upon detonation, but has been applied to relatively thick metal plates with grooves[13–15,18,19] (the geometry shown in Fig. 1). The second theory is a limiting case of RMI[4] theory applied to the geometry shown in Fig. 1 by assuming At ≈ -1 for shocks that propagate in the "heavy to light" direction.

The two theories have many commonalities. Both theories assume the metal is in a completely fluid phase, and both apply isentropic[18] and incompressible[2,16] flow approximations. Since fluid jets must have non-zero vorticity (i.e., transverse velocity shear, or, equivalently non-zero curl of the velocity field, $\nabla \times \mathbf{u} \neq 0$), both theories predict patterns of vorticity deposition at the interface generated by

pressure perturbations. (**R2b**) Both theories predict mass convergence at the groove center from the resulting pattern of vorticity deposition and, subsequently, both theories predict both jet mass and jet velocity.[6,18] Therefore, either by implicit or by explicit mathematical descriptions of the problem geometry, the epistemic view of jet formation of both theories is derived from *the same underlying baroclinic fluid physics*.[4]

We shall refer to the theories by their mathematical descriptions of vorticity deposition rather than by the names of individual contributors. Both theories have been developed for at least six decades and have many contributors. The contributors to the first theory include Birkhoff,[16] MacDougall,[16] Pugh,[16,20] Taylor,[16] Eichelberger,[20,21] Asay,[13] de Rességuier,[14] Lescoute,[14] Sollier,[14] Prudhomme,[14] Mercier,[14] Soulard,[18] and probably others. The contributors to the second theory include Meyer,[22] Blewett,[22] Dimonte,[23] Ramaprabu,[6,23] Mikaelian,[24] Zhang,[25] Velikovich,[26] Buttler,[5] Oró,[5] Preston,[5] Cherne,[5,6] Hixon,[5] Mariam,[5] Morris,[5] Stone,[5] Terrones,[5] Tupa,[5] Karkanis,[6] Hammerberg,[6] Andrews,[6] Taylor,[27] Richtmyer,[2] and probably others. For reasons that will become clear in Sec. II A, we refer to the first theory as **piecewise theory**, denoted by subscript δ because a spatially piecewise velocity profile is equivalent to a δ function in vorticity [Figs. 2(a) and 2(b)]. Similarly, we refer to the second theory as **modal theory**, denoted by subscript m, because RMI theory models the

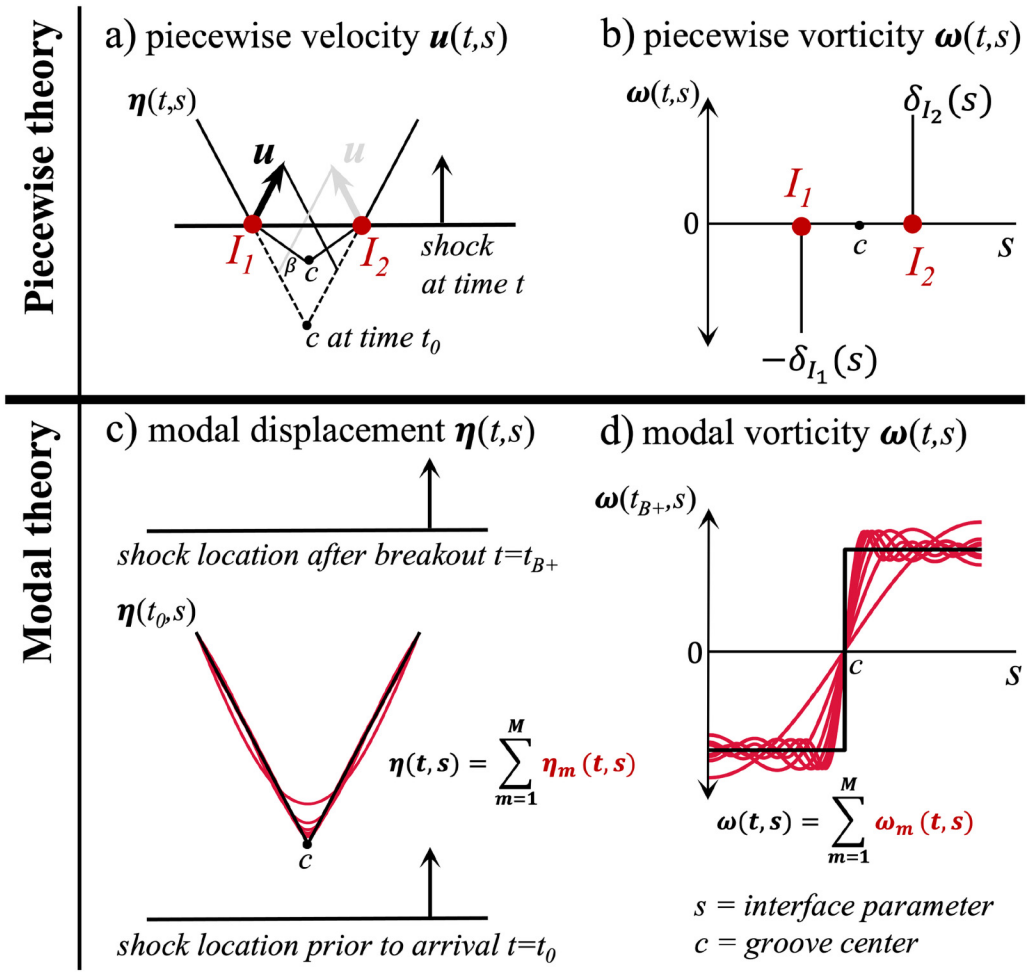

FIG. 2. Two different theories of vorticity deposition on the interface. s is a parametric coordinate for the interface position $\boldsymbol{\eta}$. In shaped charge liner theory [(a) and (b)], the free surface velocity within the groove (at points l_1 and l_2) is predicted and the fluid velocity behind the shock is treated as incompressible "plug" flow. The Bernoulli equation is applied behind the shock to estimate mass and momentum convergence at the groove center and subsequently jet mass and velocity. The vorticity model of this theory is composed of δ functions at points l_1 and l_2, where the δ functions move outward from the center as the shock propagates toward the planar free surface. In At ≈ -1 RMI theory [(c) and (d)], the interface is treated as a set of modes of displacement and velocity that are excited by the impulsive acceleration of the shock (i.e., a δ function in time). The vorticity is also a set of evolving modes. Scenario *d* is a modal approximation of *b* where non-zero vorticity residuals persist behind the δ functions, such as might happen if scale-dependent physical effects, such as viscosity, truncate the Fourier expansion of the delta functions in *b*.

deposition of vorticity at the interface in the form of periodic modes that are impulsively excited by the shock transit [Figs. 2(c) and 2(d)].

A. Velocity ratio predictions of piecewise theory

Piecewise theory originates from a theory proposed by Birkhoff *et al.*[16] for predicting jets that emerge from "wedge" shaped charges, assuming the detonation wave of the high explosive is planar and the detonation wave normal is parallel to the axis of symmetry of the wedge (i.e., groove). As a planar detonation wave (i.e., the shock) with velocity u_{sh} transits the metal liner around the groove, the reflected waves cause the free surface *within the groove* to instantaneously accelerate to a velocity that Birkhoff *et al.*[16] derived from shock reflection theory and the problem geometry. Shock reflection theory predicts that as the shock transits the groove the free surface velocity within the groove has an interface tangential component that points inward toward the groove center (denoted c in Fig. 2). To derive the theory, Birkhoff *et al.*[16] assumed that

1. the metal liner at the interface is infinitesimally thin;
2. the detonation wave/shock pressure is sufficiently large that the pre-shock solid metal liner instantaneously becomes fully fluid when shocked;
3. the fluid liner is approximately inviscid;
4. the fluid liner is approximately incompressible;
5. the pressure on either side of the fluid liner "quickly equalizes" immediately behind the shock wave such that pressure differences do not affect the liner behind the shock;
6. the fluid liner in between the shock and groove center is a plug flow: it has zero vorticity, zero velocity divergence, and zero acceleration (i.e., it is steady);
7. the fluid liner flow remains symmetric at the groove center; and
8. the fluid liner flow is isentropic.

Under these assumptions, vorticity deposition is represented as a piecewise step function in the free surface velocity within the groove. The vorticity is prescribed as exactly zero both immediately ahead of and behind the shock. No vorticity is generated outside of the groove because the planar free surface is parallel to the normal direction to the planar shock and, therefore, the entire planar surface uniformly gains velocity upon shock breakout.

Assumptions 1–8 permit the application of the steady-state Bernoulli equation to the fluid liner behind the shock, allowing for the prediction of jet velocity and mass owing to the expulsion of mass and momentum at the groove center c [Fig. 2(a)]. The expulsion is necessary to balance the mass and momentum convergence attributed to the interface tangential component of free surface velocity within the groove and the shortening of the groove interface as the interface is displaced from its pre-shock position to its position during shock transit. The convergence is shown by comparison of the dashed line in Fig. 2(a) (the pre-shock position of the interface $\boldsymbol{\eta}$) with the solid line for $\boldsymbol{\eta}$ in Fig. 2(a). The liner converges at the angle β relative to the pre-shock geometry [shown in Fig. 2(a)], where β has a constant value under the steady flow assumption (assumption 6). However, β is not analytically tractable and can be determined: (a) by direct empirical fitting[13,20,21] (denoted by subscript δ, 1); (b) by semi-empirical methods that use additional kinetic equations, an equation of state for the metal liner, and additional conservation equations[14,28] (denoted by subscript δ, 2); or (c) by relaxing the isentropic assumption and using a modified form of the Bernoulli equation appropriately coupled with the equation of state.[18]

A final assumption (not explicitly discussed by Birkhoff *et al.*[16]) is that the shock velocity tangent to the free surface inside the groove must be greater than the speed of sound behind the shock, referred to as the "regular" case.[14,18] Otherwise, the shock front is disrupted by release waves propagating from the bottom of the groove. In the latter case, referred to as the "irregular" case,[14] the propagation of both the incident shock and the reflected rarefaction waves are no longer steady and assumption 6 is violated. Semi-empirical approaches[14,18,28] for the prediction of β distinguish between regular and irregular shocks and, in doing so, delineate a cutoff for when the steady-state Bernoulli equation may be applied to liner flow behind the shock.

The velocity ratio for the wedge shaped charge jet prediction of Birkhoff *et al.* is

$$U_\delta = \frac{u_{sh}}{u_{fs}} \frac{\sin(\beta-\theta)}{\cos\theta} \left(\csc\beta + \cot\beta + \tan\left(\frac{\beta-\theta}{2}\right)\right), \tag{30}$$

where u_{sh} is the shock velocity (i.e., the detonation wave velocity of a wedge shaped charge in their work), u_{fs} is the planar free surface velocity (outside of the groove), and subscript δ denotes the piecewise model. Equation (30) is identical to Eq. (2′) in Birkhoff *et al.*[16] and Eq. (12) in Asay[13] when divided by u_{fs} and by equating the detonation wave front in the high explosive of Birkhoff *et al.*[16] with the shock velocity of a planar shock moving upward through the metal plate in Fig. 1. The jet velocity of Eq. (30) *does not* satisfy the relevant boundary conditions for shocked metal plates with grooves [Fig. 1, Eqs. (18) and (24)] because $U_\delta = 2u_{sh}/u_{fs}$ at $\theta = 0^\circ/\eta_0 k \to \infty$,[16] where

$$\frac{\sin(\beta)}{\cos(0)} \left(\csc\beta + \cot\beta + \tan\left(\frac{\beta}{2}\right)\right) = 2 \quad \forall (0 \le \beta < \pi/2), \tag{31}$$

and because $U_\delta = \infty$ at $\theta = 90^\circ/\eta_0 k = 0$, where

$$\frac{\sin(\beta-\pi/2)}{\cos(\pi/2)} \left(\csc\beta + \cot\beta + \tan\left(\frac{\beta-\pi/2}{2}\right)\right) = \infty \quad \forall (0 \le \beta < \pi/2). \tag{32}$$

Equations (18) and (24) are the statement that, regardless of assumptions 1–8, groove-driven jetting phenomena must vanish with the grooves themselves at both θ extrema.

B. Velocity ratio predictions of modal theory

Richtmyer[2] derived the earliest form of modal theory from Taylor's[27] theory of the growth of small-amplitude single-mode interface perturbations, where the interface is between two incompressible fluids under constant acceleration and a constant pressure gradient. In Richtmyer's derivation, the constant acceleration and constant pressure gradient of Taylor's theory are replaced by an impulsive acceleration representing a shock wave.

Richtmyer[2] proposed that shock driven interface instabilities propagate away from free surface defects according to

$$|\dot{\eta}_0^s| = |\eta_0 k u_{fs}|, \tag{33}$$

where $\dot{\eta}_0^s$ represents the initial RMI "spike" velocity, relative to the inertial reference frame of the moving free surface, and u_{fs} is the free surface velocity. Richtmyer invoked five assumptions to formulate Eq. (33).

1. The post-shock material is in the fluid phase or fluid-like plastic deformation and can be idealized as baroclinic vorticity.
2. The fluid is only accelerated by the shock.
3. The interface position and velocity evolve linearly, requiring the scaling $\eta_0 k \ll 1$.
4. The pre-shock geometry is effectively two dimensional, satisfying Eqs. (2) and (3).
5. The pressure behind the shock is constant.

Assumptions 1 and 5 are particularly stringent idealizations that do not strictly hold in experiments because (a) friction, compressibility, and rotational deformation occur within shocked metals and (b) pressure waves can only be approximated as constant over finite time scales. Buttler *et al.*[5] proposed several corrections to address the assumptions above for the unity Atwood number case informed by previous studies.[3,22,29–31] The reader is referred to their paper for discussion of those corrections.

To correct for Richtmyer's third assumption (linearity $\eta_0 k \ll 1$), Buttler *et al.*[5] chose a nonlinearity correction model from Dimonte and Ramaprabhu[23] in the form of an additional spatial perturbation Taylor series expansion term,

$$F_{nl,1}^s = \frac{1}{1 + (\eta_0 k/2)^2}. \tag{34}$$

However, Dimonte and Ramaprabhu[23] argued that

$$F_{nl,2}^s = \frac{1}{1 + (\eta_0 k/3)^{4/3}}, \tag{35}$$

determined by Padé approximation in Velikovich and Dimonte,[26] more closely agrees with simulation data than the correction in Eq. (34). Both nonlinearity models are examined below.

Buttler *et al.*[5] assumed that compressible and nonlinear effects act independently to propose a model of the asymptotic (i.e., late-time $t = t_\infty$) steady-state velocity of the RMI spike,

$$|\dot{\eta}_\infty^s| \approx \sqrt{3}\left(1 - \frac{u_{fs}}{2u_{sh}}\right) F_{nl}^s |\eta_0 k u_{fs}|, \tag{36}$$

where $\sqrt{3}$ maps the spike velocity $\dot{\eta}_0^s$ at shock breakout time $t = \Delta t$ to the asymptotic steady-state spike velocity $\dot{\eta}_\infty^s$.[5,24,25,32] Equation (36) is related to the velocity ratio U by

$$U = \frac{u_\infty^s}{u_{fs}} = 1 + \frac{\dot{\eta}_\infty^s}{u_{fs}}, \tag{37}$$

where $u_\infty^s = u_{fs} + \dot{\eta}_\infty^s$. The formulation in Buttler *et al.*[5] implemented with $F_{nl,1}^s$ [Eq. (34)] can be expressed as

$$U_{m,1}(\eta_0 k) = 1 + \sqrt{3}\left(1 - \frac{u_{fs}}{2u_{sh}}\right) \frac{|\eta_0 k|}{1 + (\eta_0 k/2)^2}, \tag{38}$$

$$U_{m,1}(\theta) = 1 + \sqrt{3}\left(1 - \frac{u_{fs}}{2u_{sh}}\right) \left(\frac{\pi |\cot\theta|}{\frac{1}{8}\pi^2 \cot^2\theta + 2}\right), \tag{39}$$

where subscript m denotes the modal model. The formulation in Buttler *et al.*[5] implemented with $F_{nl,2}^s$ [Eq. (35)] can be expressed as

$$U_{m,2}(\eta_0 k) = 1 + \sqrt{3}\left(1 - \frac{u_{fs}}{2u_{sh}}\right) \frac{|\eta_0 k|}{1 + (\eta_0 k/3)^{4/3}}, \tag{40}$$

$$U_{m,2}(\theta) = 1 + \sqrt{3}\left(1 - \frac{u_{fs}}{2u_{sh}}\right) \left(\frac{\pi |\cot\theta|}{\frac{\pi^{4/3}}{3\times 6^{1/3}} \cot^{4/3}\theta + 2}\right). \tag{41}$$

Equations (38)–(41) and (40) satisfy the boundary conditions of Eqs. (18) and (24).

1. Predicted maxima of velocity ratios

The local maxima of the velocity ratio in the ranges $\eta_0 = [0, \infty]$ or $\theta = [0°, 90°]$ yields an upper bound on the velocity ratio as predicted by baroclinic vorticity theory with the Taylor expansion nonlinear factor[5,23] [Eqs. (38) and (39)],

$$\max U_{m,1} = 1 + \sqrt{3} \approx 2.7, \tag{42}$$

for the limit condition $u_{fs}/u_{sh} \to 0$ and $\theta = \tan^{-1}(\pi/4) \approx 38.1°$ or, equivalently, $\eta_0 k = 2$.

For baroclinic vorticity theory with the Padé approximation nonlinear factor,[26] the upper bound on the velocity ratio is [Eqs. (40) and (41)]

$$\max U_{m,2} = 1 + \frac{9 \times 3^{1/4}}{4} \approx 4.0, \tag{43}$$

for the conditions $u_{fs}/u_{sh} = 0$ and $\theta = \tan^{-1}(\pi/(6 \times 3^{3/4})) \approx 12.9°$ or, equivalently, $\eta_0 k = 3 \times 3^{3/4} \approx 6.8$.

C. Jet mass prediction from an empirical fit

Missing mass theory is an empirical fit by Asay and Bertholf[8] over 11 jet mass experiments featuring six different materials (Al, Cu–W, Pb, Cu–Au, Au, and W), a range of shock pressures (25–36, 91, 9–15, 88, 90, and 25 GPa, respectively), a variety of defect geometries (including but not limited to grooves) with defect volumes ranging over three orders of magnitude. It is a linear regression that predicts the scaling of ejecta mass with defect volume to within a factor of three.[8] Formally,

$$J(t \to \infty) \in [1/3, 3]. \tag{44}$$

However, Asay and Bertholf varied material, shock pressure, defect geometries, and defect volume simultaneously, therefore, the experiments did not determine how each of these affects outflow mass independently.

D. Jet mass predictions from piecewise theory

To apply the theory of Birkhoff *et al.*[16] to a relatively thick plate with a groove (Fig. 1) rather than a shaped charge, the mass and momentum divergence at the groove center is only permitted to diverge (i.e., jet) out of the metal because it is blocked from moving in the opposite direction (downward in Fig. 1) by the inertia of a significant amount of subsurface metal. Therefore, the total mass of the jet is equivalent to the mass of the liner per unit length of the groove and it grows from zero at the rate determined by the interface tangent component of the velocity of the free surface within the groove.[18]

E. Jet mass predictions from modal theory

Modal theory (Sec. II B) was expanded by Cherne *et al.*[6] to predict jet areal mass (units $[M/L^2]$),

$$\rho_{A,m,1}(t) = \frac{2}{3}\rho_\star \ln\left[1 + \frac{(t-\Delta t)}{\tau(\beta_0 + \Delta t/\tau)}\right], \quad \forall t \geq \Delta t, \tag{45}$$

where subscript A denotes "areal" mass, subscript m denotes the modal model, and the subscript 1 denotes the choice of nonlinear factor [Eq. (34)]. Here,

$$\rho_\star = \frac{\rho_0 \lambda}{3\pi}, \tag{46}$$

$$\tau = \frac{\lambda}{3\pi \dot{\eta}_0^b}, \tag{47}$$

$$\frac{\Delta t}{\tau} = e^{3/2\eta_0 k F_l} - 1, \tag{48}$$

$$\dot{\eta}_0^b = F_l F_{nl,1}^b |\eta_0 k u_{fs}|, \tag{49}$$

$$F_l = 1 - \frac{u_{fs}}{2u_{sh}}, \tag{50}$$

$$F_{nl,1}^b = \frac{1}{1 + \eta_0 k/6}, \tag{51}$$

$$\beta_0 = 1 + \frac{1}{\sqrt{3}} \frac{F_{nl,1}^b}{F_{nl,1}^s}, \tag{52}$$

assuming a conservation of volume flux across the free surface and a parabolic jet shape. At $t - \Delta t = 0$, the groove has "flattened," and, therefore, $\rho_\star$ approximates the quantity of mass that fills in groove at time $t = \Delta t$, ignoring compressibility, phase effects, and other phenomena. Equation (45) satisfies the boundary conditions of Eqs. (19) and (25). Equation (45) can also be expressed in the form of the areal jetting factor per unit length [Eq. (13)],

$$J_{A,m,1}(t) = \frac{2\lambda}{9\pi A_{xy}} \ln\left[1 + \frac{(t-\Delta t)}{\tau(\beta_0 + \Delta t/\tau)}\right], \quad \forall t \geq \Delta t. \tag{53}$$

III. SYNOPSIS OF RELEVANT EXPERIMENTAL DATA

Table I documents the salient characteristics of previously reported experiments. The reader is referred to the references provided in column 1 of Table I for the methodological details of each experiment. To enhance the reproducibility and inter-comparability of future experiments, we recommend that future experiment reports include a similar table. All u_{fs}/u_{sh} values with the dagger symbol † in Table I were calculated by using Rankine–Hugoniot tables[33] and the relevant reported variables (e.g., u_{fs}, P_{SB}, and ρ_0) in each study. Velocity ratio and areal masses were reported in Antipov *et al.*[34] (An17) for double-mode triangular grooves. $\eta_0 k$ and θ were calculated for the groove cross-sectional geometry shown in An17's Fig. 3. Data were used from An17's "collision zone" (higher pressure region of the shocked target) measurements in Tables 2 and 4. In the experiments of An17 and Hammerberg *et al.*[35] (Ha18) the grooves were milled in circles on the free surfaces of the targets and not straight lines [footnote (a) in Table I]. All other reported grooves are linear.

Velocity ratios and areal masses were reported in (As76) of Ref. 13 in their Table 4 and Fig. 21, with additional groove geometry details provided in their Table 3. Instead of shock breakout pressures, As76 reported flyer impact pressures [footnote (b)], which are shown in Table I. Asay and Bertholf[8] (As78) reported areal masses and groove geometry in their Table 4. Buttler *et al.*[5] (Bu12) reported velocity ratios and groove geometry in their Tables 1 and 2. Buttler *et al.*[36] (Bu21) examined mass outflows that chemically react in response to gases above the free surface. They reported velocity ratios and areal masses for two non-reactive experiments [footnote (c) in Table I] in which mass outflows from defects into a vacuum ("Sn2" and "Ce1") in their Table 1 and Fig. 3. Bober *et al.*[37] reported velocity ratio data and groove geometry for Sn and Cu in their Table 1. Two out of six shots were reported as fully fluid phase and the others produced jets. They held the groove half-angle constant for all six experiments. They attempted to keep the groove width constant (approximately 290 μm) but reported some variability in the exact groove widths. We averaged the groove cross-sectional areas for each material.[(j)]

Frachet *et al.*[38] (Fr88) report velocity ratios for different shock drives and a range of shock breakout pressures, but they did not specify the drive type chosen, nor shock breakout pressure, for each reported experiment.[(d)] They reported only groove half angles without specifying groove depth or width, and, therefore, groove cross-sectional areas could not be calculated.[(e)] They report velocity ratio experimental data in their Fig. 9. Fr88 did not report sufficient information to independently estimate the phase[39] of the shocked metals in their experiments. Ha18 reported velocity ratios and areal masses in their Table 1 and Fig. 4. We assume that the latest time areal mass reported in their Fig. 4 is the total areal mass. However, their experiments included helium at 7 atm pressure above the free surface[(f)]. Jensen *et al.*[40] (Je15) reported velocity ratios as a function of effective sinusoidal groove geometry in their Table 1. The shock pressure in their target was not sufficiently high for fully fluid phase; their target was likely in solid state plastic deformation. Their estimates of groove wavelength λ include flat free surface gaps between grooves that are wider than the grooves themselves. Their groove cross-sectional geometry was semi-circular[(g)].

TABLE I. Planar shock experiments on groove defects. Not Available (NA) indicates that the data were not reported in an unambiguous manner. Shock loading in the target is driven by high explosives (HE), flyer plate impacts (I), or laser pulses (L). For triangular and sinusoidal defects, the cross-sectional area is $A_{xy,\mathrm{tri}} = \eta_0\lambda$ and $A_{xy,\mathrm{sine}} = \eta_0\lambda/\pi$, respectively.

Study	Target	Drive	P_{SB} (GPa)	Shape	$\eta_0 k$ (rads)	θ (degrees)	u_{fs}/u_{sh}	A_{xy} (μm^2)
An17[34]	Pb	HE	42.5	Triangular[a)]	0.69	66.25	0.50	4400
As76[13]	Al	I	29.4–29.6[b)]	Triangular	1.57–11.93	7.50–45.00	0.41	390-2330
As78[8]	Al	I	30	Triangular	1.71–8.75	10.18–42.65	NA	450-2300
As78[8]	Cu–Au	I	88	Triangular	3.64	23.34	NA	1400
Bo21[37]	Sn	I	6.9–34.2	Triangular	2.61	31.0	0.20–0.55†	36 000[j)]
Bo21[37]	Cu	I	26.8–55.9	Triangular	2.61	31.0	0.26–0.41†	33 000[j)]
Bu12[5]	Sn	HE	22,27	Sinusoidal	0.12–2.00	38.14–85.63	0.47	2020–5490
Bu12[5]	Cu	HE	36	Sinusoidal	0.12–1.50	46.32–85.63	0.31	2020–5490
Bu21[36c)]	Sn	HE	28.3	Sinusoidal	0.33	77.79	0.48†	30
Bu21[36c)]	Ce	HE	18.3	Sinusoidal	0.36	77.44	0.71†	190
Fr88[38]	Cu	NA[d)]	10–120	Triangular	0.28–5.77	15.23–79.88	NA[d)]	NA[e)]
Ha15[35f)]	Sn	HE	25	Sinusoidal[a)]	0.50	72.34	0.44–0.46†	101 220
Je15[40]	Ce	I	5.3–7.6	Sinusoidal[g)]	0.70–1.04	56.37–65.94	0.44–0.50†	7420–11 060
Mi14[41]	Pb	HE	7–23	Sinusoidal	0.63–0.97	58.39–68.2	0.41–0.83	40–13 240
Mn14[42]	Sn	HE	27	Sinusoidal	0.07–1.68	43.06–87.62	0.46[h)]	3–890
Pr20[43]	Sn	L	42–49	Sinusoidal	0.38–1.23	51.9–76.4	0.58	70–670
Re14[14]	Sn	L	6.5–28.6	Triangular	5.44,3.14	30.0,45.0	0.15–0.44†	870–980[k)]
Re14[14]	Al	L	9.6–24.7	Triangular	5.44,3.14	30.0,45.0	0.13–0.33†	980–1040[k)]
Vg05[11]	Sn	HE	26–28	Triangular	0.08–1.57	45.00–87.00	0.46–0.48†	2–230
Xi19[7i)]	Sn	L	25–29.1	Triangular	0.91–2.72	30.00–60.00	0.41–0.49†	1040–3120
Ze08[12]	Sn	HE	16–28.5	Triangular	0.08–1.52	46.00–87.00	NA	8–760

[a)]Experiments of circular, rather than linear grooves, on shocked metal surfaces.
[b)]Reported pressures are flyer impact pressures and not breakout pressures.
[c)]Experiments with a vacuum-metal interface rather than a gas-metal interface.
[d)]Shock drive type not reported and it is unclear if the reported pressures are shock breakout pressures.
[e)]Insufficient information was reported for the estimation of groove cross-sectional areas.
[f)]Experiments of gas-metal interfaces with the pre-shock gas at 7 atm of pressure.
[g)]Groove cross-sectional shapes are semi-circular approximations of sinusoids.
[h)]Ratios of free surface velocity to shock velocity were estimated from reported analytical solutions.
[i)]Areal masses were estimated by dividing the reported masses by cross-sectional areas estimated from reported groove dimensions.
[j)]Averaged groove cross-sectional areas.
[k)]Groove cross-sectional areas estimated from reported cross-sectional images.

Mikhailov *et al.*[41] (Mi14) report areal masses and velocity ratios in their Table 2. They report groove geometry in their Table 1, where their roughness parameter is approximately equivalent to the defect depth, $R_z \approx h_0 = 2\eta_0$. Monfared *et al.*[42] (Mn14) report areal masses and velocity ratios in their Figs. 12/14 and Table 5, respectively. We estimated the ratio of free surface velocity to shock velocity u_{fs}/u_{sh} by choosing the appropriate value of u_{fs}/u_{sh} such that Eqs. (38) and (39) yield identical theoretical predictions to those reported in their Table 5$^{(h)}$. Prudhomme *et al.*[43] reported areal masses and the velocity ratio data in their Table 1. We use their estimate of the jet tip velocity from x-ray radiography which represents "the velocity of a front containing 99% of the ejected mass." de Rességuier *et al.*[14] report velocity ratio data in their Table 1. They reported groove half angles but did not provide depth or width, therefore, we used their Fig. 2 to infer depths of 66 μm (Al 20°), 60 μm (Al 30°), 55 μm (Sn 30°), and 44 μm (Sn 45°). To estimate the depths of their Sn 20° and Al 45° grooves we used the depths estimated from their Fig. 2 for the Al 20° and Sn 45° grooves, respectively. Therefore, the groove cross-sectional areas we report for de Rességuier *et al.*[14] are uncertain approximations.$^{(k)}$ We assumed de Rességuier *et al.*[14] used aluminum 6061 to calculate u_{fs}/u_{sh} from Rankine–Hugoniot tables.[33] Vogan *et al.*[11] (Vg05) report velocity ratios and areal masses in their Fig. 5/Table 1 and Fig. 11, respectively. Xin *et al.*[7] report velocity ratios and outflow masses in their Tables 1 and 2, respectively. Areal masses were computed by dividing the outflow masses by the cross-sectional areas of the constant-depth groove geometries detailed in their Fig. 1$^{(i)}$. Zellner *et al.*[12] report a summary of previously reported areal masses in their Fig. 5 and Table 2.

IV. VELOCITY RATIO MISSING EXPERIMENTS

Figure 3 depicts the observed velocity ratios of many of the experiments in Table I, piecewise theory for constant collapse

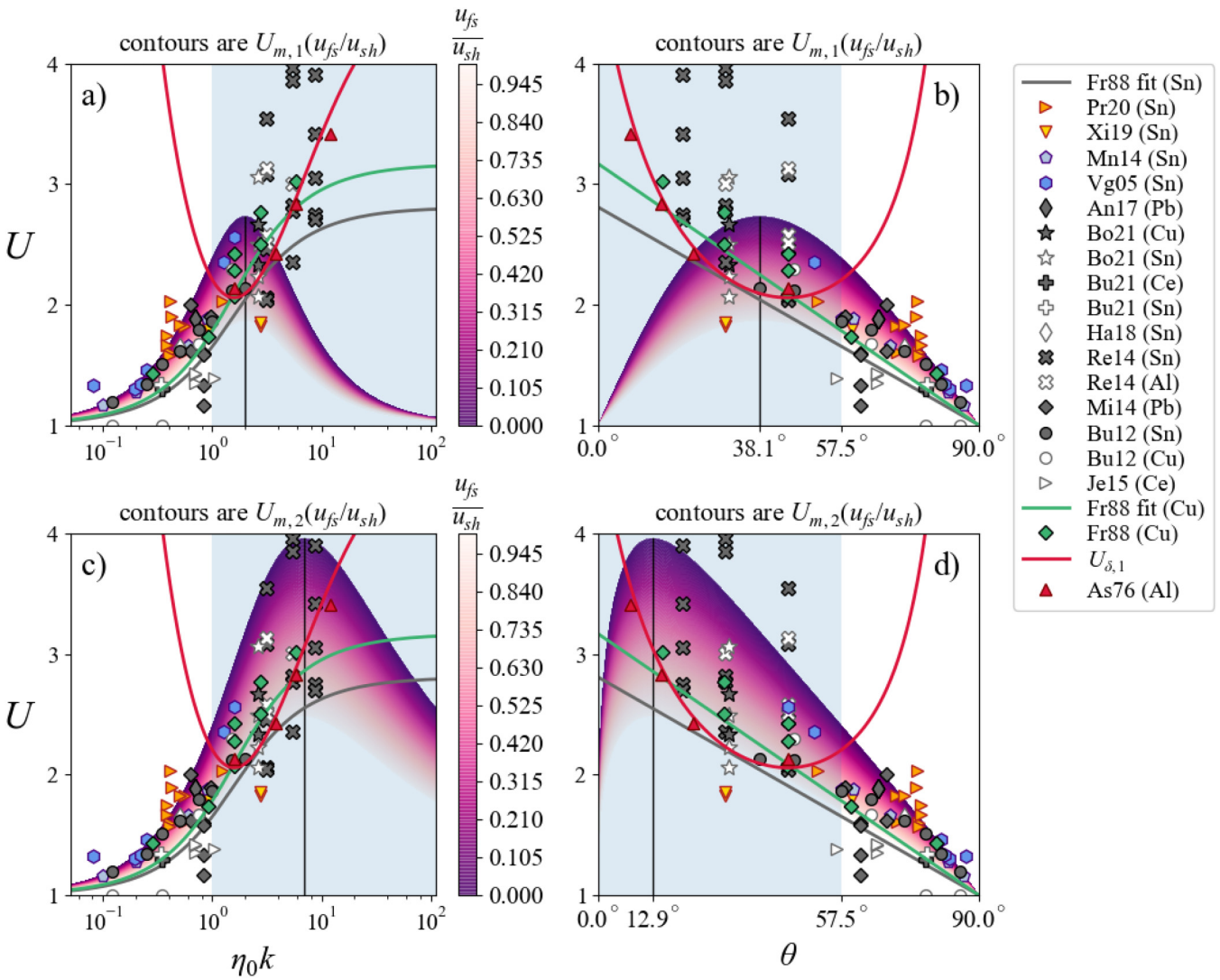

FIG. 3. The velocity ratio, U, the ratio of the jet tip velocity (equivalent to RMI spike tip velocity) to the free surface velocity, as a function of $\eta_0 k$ [(a) and (c)] and θ [(b) and (d)]. The shaded blue region indicates the nonlinear regime[26] characterized by $\eta_0 k > 1$ initial conditions, while the black vertical lines indicate the $\eta_0 k, \theta$ values of the modal theory maxima. The velocity ratio predictions of modal theories [Eqs. (38)–(41)] are shown in the purple/pink contours, where the contours represent the value of u_{fs}/u_{sh} ($u_{fs}/u_{sh} = 0$ and 1 are the upper and lower bounds, respectively). The green, solid black, and dashed black lines represent empirical fits by Frachet *et al.*[38] to Cu, Sn, and Ta experimental data. The red line shows the piecewise theory [Eq. (30)] when computed for the experiment (red triangles) parameters of Asay[13] and using Asay's prescribed liner collapse angle of $\beta = \theta + 20°$ for all θ (subscript δ, 1). The velocity ratio set of missing experiments is characterized by increasing sparsity in the number measurements of velocity ratios as $\eta_0 k/\theta$ increase/decrease, respectively. The acronyms in the legend correspond to the experiments shown in Table I. The experiments span a diverse set of pressures, materials, and drives.

angle $\beta = \theta + 20°$[13] [red line, Eq. (30)], the empirical fits of Frachet *et al.*[38] (green and gray lines), and both forms of modal theory [Eqs. (38) and (39) in the top row and Eqs. (40) and (41) in the bottom row], which are shown with purple/pink contours. The expanded range of θ and $\eta_0 k$ in Fig. 3, as well as the incompatibility of piecewise theory for constant collapse angle β with the relevant boundary conditions [Eqs. (18) and (24)], suggests that piecewise theory for constant collapse angle β is inapplicable to the physics of shocked grooves in metal surfaces and the agreement reported in Asay[13] is an artifact of inadequately sampling the variability of the velocity ratio across θ or $\eta_0 k$. The empirical fits of shocked groove defect experiments in tin and copper by Frachet *et al.*,[38] shown for completeness, also do not satisfy the boundary condition at $\theta = 0°$, $\eta_0 k \to \infty$, where $U = 0$ [Eq. (24)] because there is no groove. However, the empirical fits reasonably agree with the overall trend of

experiments in a variety of metals for $\theta > 12.9$ or, equivalently, $\eta_0 k < 6.8$. The spread of the modal theory that includes the Padé approximation nonlinear correction [Eqs. (35), (40), and (41)] from Dimonte AND Ramaprabhu[23] [Figs. 3(c) and 3(d)] agrees better with experimental data points at high $\eta_0 k$ [Figs. 3(a) and 3(b)] than with the modal theory including the Taylor expansion nonlinear term [Eqs. (34), (38), and (39)] due to the denominator in Eq. (35).

de Rességuier *et al.*[14] reported the necessary variables for the calculation of modal theory (u_{fs}, P_{SB}, $\eta_0 k$, and/or θ), calculations of piecewise theory predictions for variable β estimated from semi-empirical methods (denoted by subscript $\delta, 2$), and experiment observations. Using their Table 1, we directly compare of $U_{m,1}$, $U_{m,2}$, and $U_{\delta,2}$ with experiments using percent error,

$$\%\text{error} = \frac{U_{\text{theory}} - U_{\text{exp.}}}{U_{\text{exp.}}} \times 100, \tag{54}$$

and root mean square deviation of the error,

$$\text{RMSD} = \sqrt{\frac{1}{N_s}\sum_{i=1}^{N_s}(U_{\text{theory},i} - U_{\text{exp.},i})^2}, \tag{55}$$

where N_s is the number of samples. The percent error as a function of θ, $\eta_0 k$, P_{SB}, and u_{fs}/u_{sh} are plotted for all three velocity

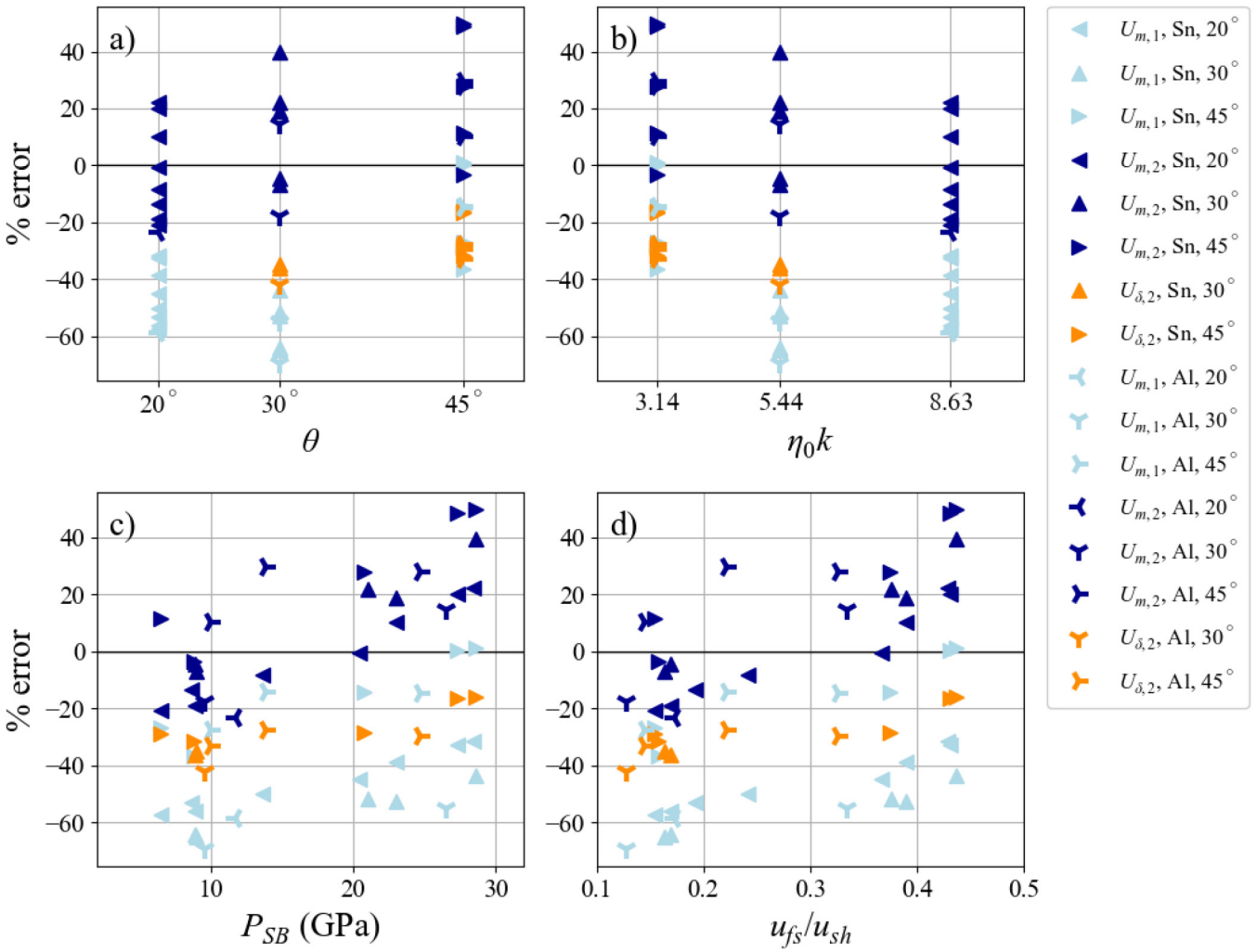

FIG. 4. The percent error of predicted velocity ratios for modal theory 1, modal theory 2, and piecewise theory 2 for both Al and Sn experiments by de Rességuier *et al.*[14] Percent error is calculated using Eq. (54). The shock velocity u_{sh} (necessary for modal theory predictions) for each experiment was estimated by using the values of P_{SB} reported by de Rességuier *et al.* and the appropriate Rankine–Hugoniot tables[33] for each material.

TABLE II. Root mean standard deviation (RMSD) error calculated using the data reported in Table 1 of de Rességuier *et al.*[14] Only values for regular flow[14] are used here because $U_{\delta,2}$ theory does not predict the existence of jets for irregular flow: the RMSD error is calculated for the same samples for each theory.

Theory	Al	Sn
Modal theory 1 ($U_{m,1}$)	1.667	1.477
Modal theory 2 ($U_{m,2}$)	0.679	0.627
Piecewise theory 2 ($U_{\delta,2}$)	1.210	0.973

ratio predictions relative to the experiment data of de Rességuier *et al.* in Fig. 4. In all four subplots, the second modal theory (Padé approximation nonlinear correction) overpredicts the velocity ratio for the majority of samples while the first modal theory (Taylor series approximation nonlinear correction) and the piecewise theory with semi-empirical methods for estimating the collapse angle underpredict the velocity ratio for the majority of samples. Table II indicates that the second modal theory is the most accurate over all of the

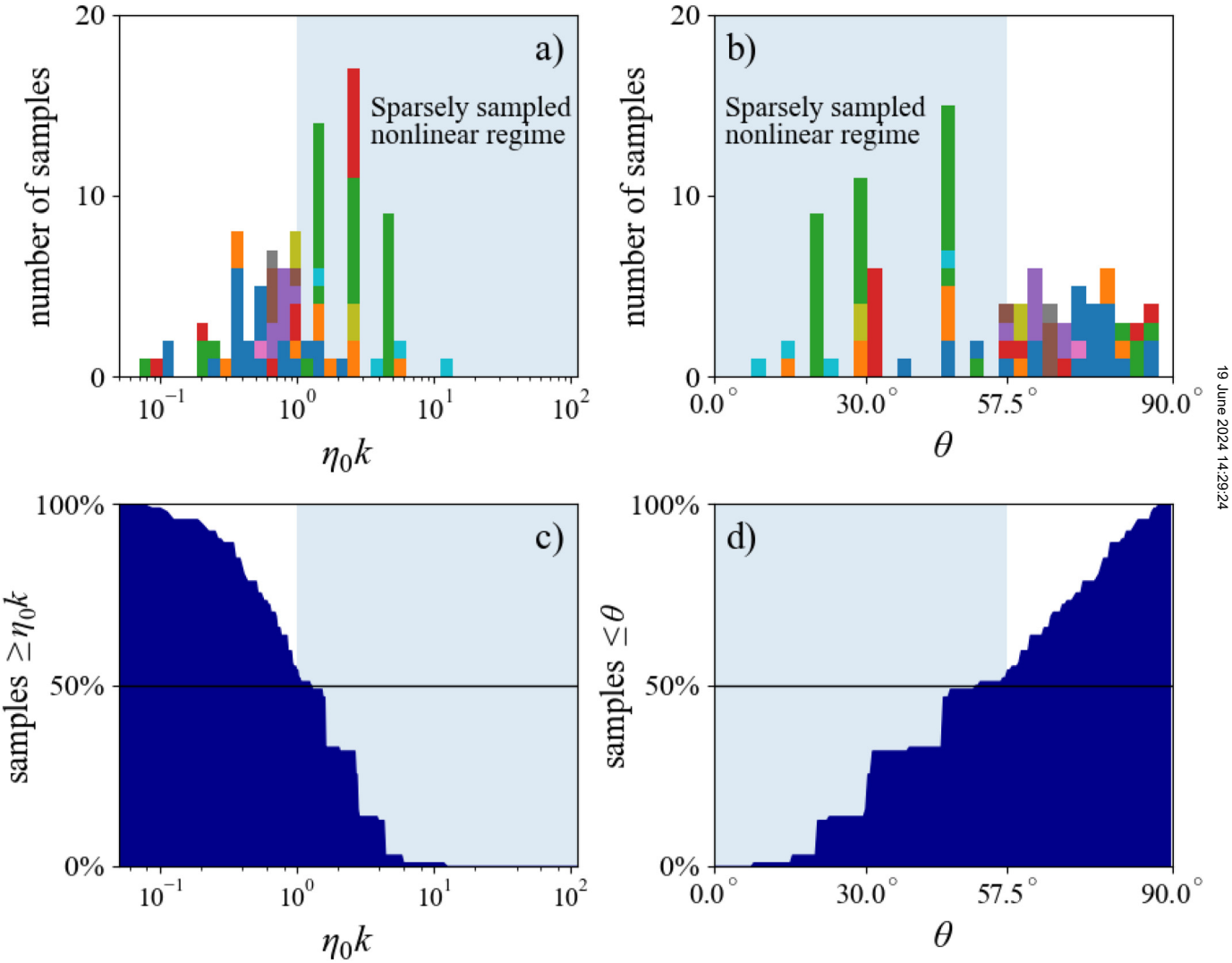

FIG. 5. The first set of missing experiments: there are sparse observations of jet velocities for the nonlinear regime:[26] groove half angles $\theta \leq 57.5°$ or, equivalently, groove $\eta_0 k \geq 1$. The histogram bars in (a) and (b) are colored by study, revealing that approximately 1/3 of all studies have examined the nonlinear regime. While approximately 50% of all experiments investigate the nonlinear regime, the sampling of $\eta_0 k$ and θ is sparse in the nonlinear regime and the 50% of experiments were performed by relatively independent studies. The total number of samples is $N_{obs} = 94$.

experiment data of de Rességuier *et al.* for both Al and Sn. However, 24 samples over three values of θ and $\eta_0 k$ from a single study are not sufficient criteria to draw the conclusion that one theory is truly the more predictive than the others for a broad range of conditions.

A. Summary of the missing velocity ratio experiments

The set of missing velocity ratio experiments is characterized by the sparsity of experimental measurements and reduced number of independent studies in the nonlinear regime,[26] shown in Fig. 5 as the shaded areas $\eta_0 k > 1$ and $\theta < 57.5°$. While Figs. 5(c) and 5(d) show that approximately 50% of all velocity ratio experiments have occurred in the nonlinear regime, Figs. 5(a) and 5(b) show that only approximately 1/3 of experimental studies have examined the nonlinear regime. New and reproduced experiments in the nonlinear regime are necessary to reduce experimental uncertainty, to reveal the variability of U for narrow and/or deep grooves, to conclusively determine which theory (Figs. 3 and 4, Table II) is more predictive, and ultimately to answer Question 1 in Sec. I.

V. OUTFLOW MASS MISSING EXPERIMENTS

There are two issues that arise when examining the variability of jet mass as a function of θ or $\eta_0 k$.

A. Jet mass confounding

Experiments are needed to assess the statistics of jet mass, m, as a function of groove aspect ratio, α, independently of other parameters. Assuming all other experimental conditions are equal, a series of experiments in which α is varied while groove volume, V, or groove cross-sectional area, A_{xy}, are held constant would provide an independent measurement of $m(\alpha)$ that is not confounded by other factors.

The jet mass is a function of groove volume; aspect ratio; other variables affected by groove aspect ratio (such as an equation of state variability as a function of half angle[44]); and other variables that are unaffected by groove aspect ratio. We can express this hypothesis in terms of θ as

$$m = m(V(A_{xy}(\theta)), \alpha(\theta), f_i(\theta), f_j(\cdot)). \tag{56}$$

Equation (56) and the following derivation could be identically expressed for $\eta_0 k$, where $i = [1, \ldots, N_i]$ and $j = [1, \ldots, N_j]$, and where N_i is the number of variables affected by the geometry of the groove (excluding V, A_{xy}, α) and N_j is the number of variables unaffected by the geometry.

Suppose an experiment is designed such that $f_i(\cdot))$ and $f_j(\cdot)$ are constant with respect to θ. Eq. (56) reduces to

$$m = m(V(A_{xy}(\theta)), \alpha(\theta)), \tag{57}$$

and the components that contribute to the variability of $m(\theta)$ is illuminated by the chain rule,

$$\frac{dm}{d\theta} = \frac{\partial m}{\partial A_{xy}}\frac{\partial A_{xy}}{\partial \theta} + \frac{\partial m}{\partial \alpha}\frac{\partial \alpha}{\partial \theta}, \tag{58}$$

where we have assumed that the groove length L_z is constant ($\partial L_z/\partial\theta = 0$). To isolate the dependence of $dm/d\theta$ on groove aspect ratio, α, the first term on the right hand side of Eq. (58) must be set to zero by experiment design. Groove cross-sectional areas should be chosen such that (for any shape groove)

$$\frac{dA_{xy}}{d\theta} = 0. \tag{59}$$

Applying Eqs. (59) to (8) and (9) yields a single symmetric groove experiment design constraint,

$$\lambda\frac{d\eta_0}{d\theta} = -\eta_0\frac{d\lambda}{d\theta}, \tag{60}$$

where groove half depth $\eta_0 > 0$ and groove width $\lambda > 0$, that applies to both triangular and sinusoidal grooves. Equation (60) is a design constraint intended to isolate the effects of groove half angle on jetting from the effects of groove volume on jetting assuming all other experimental parameters are held constant.

B. Areal jetting factor confounding

The variability of the jetting factor as a function of groove aspect ratio is confounded by groove volume variability if groove volume is not held constant as aspect ratio is varied. Since the majority of experimental investigations report jet mass in terms of areal mass, ρ_A, and since groove length, L_z, is generally held constant, we will demonstrate how the variability of the jetting factor per unit length, J_A, [Eq. (13)] with respect to groove aspect ratio can be confounded. Choosing θ as our measure of groove aspect ratio (again, the following can be identically derived for $\eta_0 k$) and

TABLE III. Exact and approximate definitions of cross-sectional area ($A_{xy,\mathrm{tri}} = \eta_0\lambda$, $A_{xy,\mathrm{sine}} = \eta_0\lambda/\pi$) as functions of θ and $\eta_0 k$ for triangular and sinusoidal grooves that do not satisfy Eq. (59). Here, $\tan\theta = \lambda(4\eta_0)^{-1}$ and $h_0 = 2\eta_0$.

Formulation of area A_{xy}	$A^{-1}_{xy,\mathrm{tri}}(\theta)$	$A^{-1}_{xy,\mathrm{tri}}(\eta_0 k)$	$A^{-1}_{xy,\mathrm{sine}}(\theta)$	$A^{-1}_{xy,\mathrm{sine}}(\eta_0 k)$
(A) Exact function of η_0, θ, k	$(4\eta_0^2\tan\theta)^{-1}$	$\eta_0 k(2\pi\eta_0^2)^{-1}$	$\pi(4\eta_0^2\tan\theta)^{-1}$	$\eta_0 k(2\eta_0^2)^{-1}$
(B) $\eta_0 \approx$ constant (constant depth)	$\sim\cot\theta$	$\sim\eta_0 k$	$\sim\cot\theta$	$\sim\eta_0 k$
(C) Exact function of η_0, θ, λ	$(4\tan\theta)\lambda^{-2}$	$(\eta_0 k)^{-1}2\pi\lambda^{-2}$	$(4\pi\tan\theta)\lambda^{-2}$	$(\eta_0 k)^{-1}2\pi^2\lambda^{-2}$
(D) $\lambda \approx$ constant (constant width)	$\sim\tan\theta$	$\sim(\eta_0 k)^{-1}$	$\sim\tan\theta$	$\sim(\eta_0 k)^{-1}$

applying the chain rule to Eq. (13) yields

$$\frac{\partial J_A}{\partial \theta} = \frac{1}{\rho_0 A_{xy}} \frac{\partial \rho_A}{\partial \theta} - \frac{\rho_A}{\rho_0 A_{xy}^2} \frac{\partial A_{xy}}{\partial \theta}. \tag{61}$$

An expression similar to Eq. (61) can be derived for the jetting factor, J. Sets of experiments that vary aspect ratio α but do not satisfy Eq. (59) (or its equivalent form for $\eta_0 k$) will produce jetting factors confounded by the variability of A_{xy} as a function of θ or $\eta_0 k$, as shown in Table III. The second term of the right hand side of Eq. (61) must be set to zero [satisfying Eq. (59)] by experiment design to assess the effect of groove aspect ratio, α, on jet areal mass, ρ_A, *independently* of groove cross-sectional area, A_{xy}. Table III shows exact and approximate forms of the variability of $1/A_{xy}$ as functions of θ and $\eta_0 k$. Rows (B) and (D) in Table III show how A_{xy} scales as a function of θ or $\eta_0 k$.

Consider an experiment in which jet mass, m, groove length, L_z, and groove depth, h_0, happen to be constant as θ or $\eta_0 k$ is varied,

$$\frac{\rho_A(\theta)}{\rho_0} \sim \text{constant} \quad \forall \theta, \tag{62}$$

$$J_A(\theta) \sim \frac{1}{A_{xy}(\theta)} \quad \forall \theta, \tag{63}$$

and Eq. (59) is *not* satisfied,

$$\frac{dA_{xy}}{d\theta} \neq 0. \tag{64}$$

The geometry shown in Table III row (B) predicts

$$J_A(\theta)|_{m,\lambda,L_z} \sim \cot\theta, \tag{65}$$

$$J_A(\eta_0 k)|_{m,\lambda,L_z} \sim \eta_0 k. \tag{66}$$

Consider a second experiment in which jet mass, m, groove length, L_z, and groove width λ happen to be constant as θ or $\eta_0 k$ is varied. The geometry shown in Table III row (D) predicts

$$J_A(\theta)|_{m,h_0,L_z} \sim \tan\theta, \tag{67}$$

$$J_A(\eta_0 k)|_{m,h_0,L_z} \sim (\eta_0 k)^{-1}. \tag{68}$$

Equations (65)–(68) predict how jetting factor variability is confounded when Eq. (59) is not satisfied by experiment design.

C. Summary of the outflow mass missing experiments

Figure 6 shows the jetting factor per unit length, J_A, as functions of $\eta_0 k$ and θ from previously reported experiment data. The reported groove geometries from these studies and overlays of the predicted variability of J_A [Eqs. (65)–(68)] indicate that none of the plotted experiments varied aspect ratio independently of defect volume. Experiments of two different aspect ratios by Xin *et al.*[7] held h_0 constant and J_A estimated from their study follow the red solid line trends predicted by Eqs. (65) and (66). Experiments by Monfared *et al.*,[42] Vogan *et al.*,[11] and Zellner *et al.*[12] varied both h_0 and λ at once. Their results follow a noisy trend more consistent with approximately holding width λ constant, where the dashed blue lines show the trends predicted by Eqs. (67) and (68).

The jetting factor per unit length predicted by baroclinic vorticity theory [Eq. (53)] is shown as a light blue dashed-dotted line in Fig. 6. The parameters of the experiment "Sn2" in Buttler *et al.*[36] were used to compute Eq. (53) such that Eq. (59) is satisfied for all aspect ratios by fixing the value A_{xy} at the value reported for $\eta_0 k = 0.34$ ($\lambda_0 = 39.2\,\mu$m, $\eta_0 = 2.05\,\mu$m, thus, the constant sinusoidal cross-sectional area is $A_{xy,0} = \eta_0 \lambda_0/\pi = 26.6\,\mu\text{m}^2$). The value of λ was varied in Eq. (53) according to

$$\lambda = f(\eta_0 k) = \sqrt{\frac{2\pi A_{xy,0}}{\eta_0 k}}. \tag{69}$$

Using the values $u_{fs} = 1920\,\mu$m/μs and $u_{fs}/u_{sh} = 0.75$, reported in Buttler *et al.*,[36] and choosing time $t - \Delta t \approx h_{\text{pin}}/u_{fs} = 15.6\,\mu$s (the measuring pin height $h_{\text{pin}} = 30$ mm[36] above the initial surface position divided by the free surface velocity), we found a profile of $J_{A,1}$ consistent with the $\eta_0 k = 0.34$ "Sn2" experiment of Buttler *et al.*[36] Thus, the light blue dashed-dotted line in Fig. 6 is a hypothesis of jetting factor per unit length variability as a function of groove aspect ratio *independent* of groove volume variability. While none of the experiment J_A data appear to satisfy $J_A \to 0$ as $\theta \to 90°$ or $\eta_0 k \to 0$ [Figs. 6(a) and 6(b)], baroclinic vorticity theory [Eq. (53)] predicts a peak followed by a rapid drop off of J_A as $\theta \to 90°$ or $\eta_0 k \to 0$ [Figs. 6(c) and 6(d)].

The missing set of outflow mass experiments is the lack of experiments that satisfy Eq. (59) as θ or $\eta_0 k$ are varied, shown in Fig. 7. Thus, the variability of jet mass as a function of θ or $\eta_0 k$, independent of groove volume, is empirically unknown. Figure 7 shows the groove cross-sectional areas A_{xy} from reported values of η_0, λ, and/or θ for the experiments in which θ was varied by at least 20°. The solid lines in Figs. 7(a) and 7(b) represent linear regressions of A_{xy} and are a conservative (i.e., smoothed) estimate of A_{xy} variability. Figures 7(c) and 7(d) show the percent difference from left to right of A_{xy}^{-1} (from minimum $\eta_0 k$ and θ to maximum $\eta_0 k$ and θ). In Fig. 7(c),

$$\%\text{difference} = 10^2 \left(\frac{A_{xy}^{-1}(\eta_0 k) - A_{xy}^{-1}(\min[\eta_0 k])}{A_{xy}^{-1}(\min[\eta_0 k])} \right), \tag{70}$$

which is applied to the regression lines in Fig. 7(a). In Fig. 7(d),

$$\%\text{difference} = 10^2 \left(\frac{A_{xy}^{-1}(\theta) - A_{xy}^{-1}(\min[\theta])}{A_{xy}^{-1}(\min[\theta])} \right), \tag{71}$$

which is applied to the regression lines in Fig. 7(b). Figures 7(c) and 7(d) show that the variability of J_A with respect to groove aspect ratio in previous experiments is confounded by factors as large 300% because the groove aspect ratio was not varied independently of groove volume.

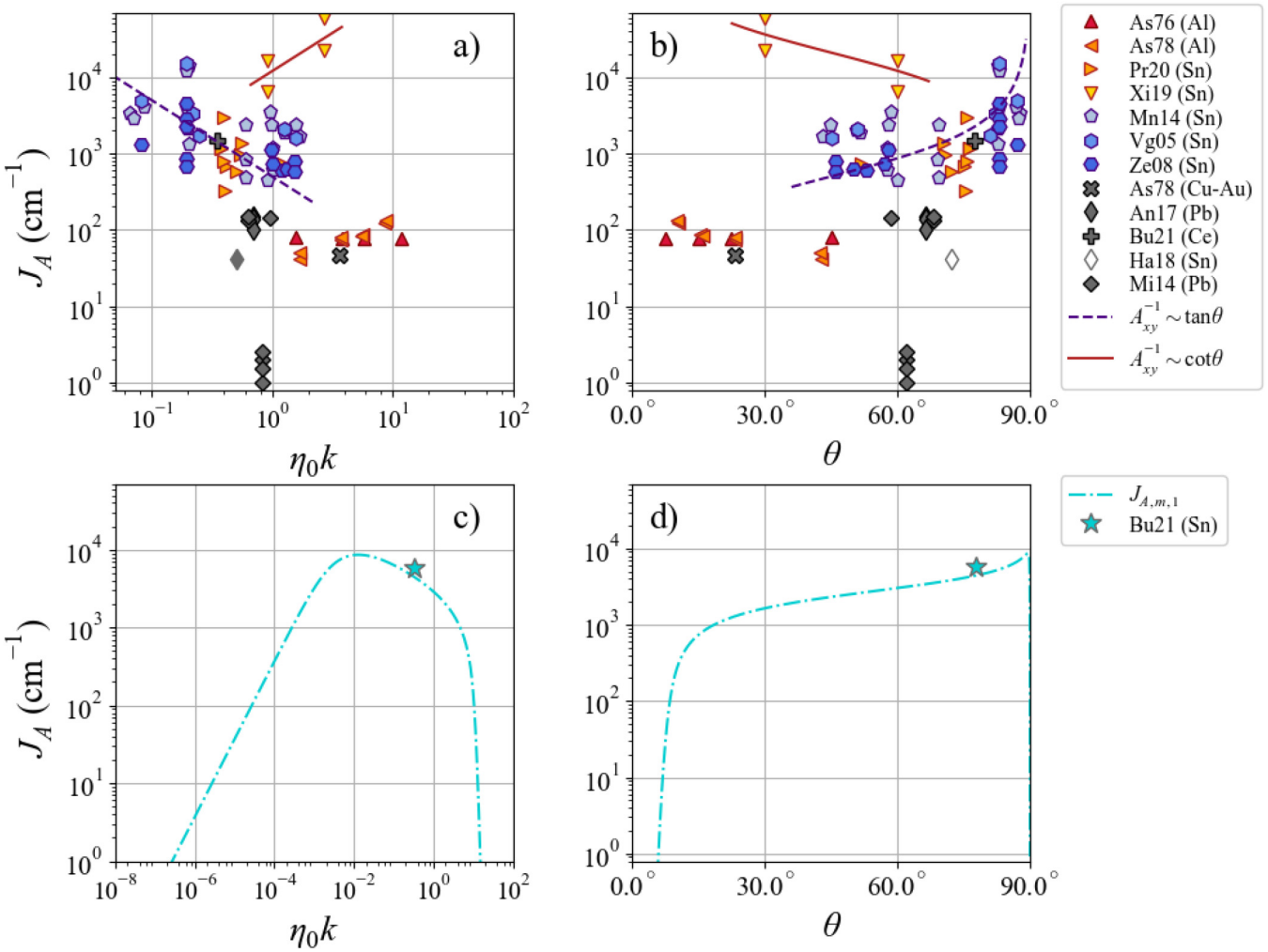

FIG. 6. Areal jetting factor per unit length of groove [Eq. (13)] computed from available experiments. The acronyms in the legend correspond to the studies detailed in Table I. The experiments were conducted using different shocked target materials and different shock pressures. Thus, we are concerned with the variability across sets of experiments by the same study, which tend to hold materials and pressures approximately constant, rather than the magnitude of J_A. The solid red line is an overlay of the constant-depth approximation (assuming constant jet mass) as shown in Table III, and the blue dashed line is an overlay of the constant width approximation (assuming constant jet mass) as shown in Table III. J_A must vanish at $\theta = 90°, \eta_0 k = 0$ and $\theta = 0°, \eta_0 k \to \infty$ because the groove itself vanishes at these limits. The baroclinic vorticity theory prediction for areal jetting factor per unit length, $J_{A,1}$ [Eq. (53)], is calculated to satisfy Eq. (59) (holding cross-sectional area constant) by using the "Sn2" experiment parameters of Buttler *et al.*[36] and is shown by the teal dashed-dotted line and the teal star, respectively.

VI. OUTLOOK: FILLING IN THE GAPS

Given the analyses presented here, we advocate for a statistically significant number of experiments to fill the two experimental gaps. The first set of missing experiments is indicated by Fig. 5. It is characterized by the increasing sparsity in the number of empirical measurements with decreasing groove half angle θ or, equivalently, increasing groove amplitude wavenumber $\eta_0 k$, and by the fact that only approximately 1/3 of all independent studies have examined the nonlinear regime ($\theta < 57.5°$, $\eta_0 k > 1$). To reduce uncertainty and conclusively rank theoretical predictions for velocity ratios (U, shown in Figs. 3 and 4) and for areal jetting factor per unit length, J_A (Fig. 6), more measurements of jet velocity and/or jet mass in the nonlinear regime are necessary. (**R2c**) Jets for low θ and high $\eta_0 k$ and lower breakout pressures are a particularly severe test of piecewise theory because it predicts no jet formation; thus, repeated observations of jets where no jets are predicted may be used to argue the falsification[45] of piecewise theory because the underlying model of vorticity deposition (Fig. 2) may not sufficiently describe the actual interface dynamics in the nonlinear regime. (**R1b**) Moreover, future experimental studies should compare calculations of each theory [$U_{m,1}$, $U_{m,2}$, $U_{\delta,2}$, (**R2b**) Soulard's piecewise model] and/or

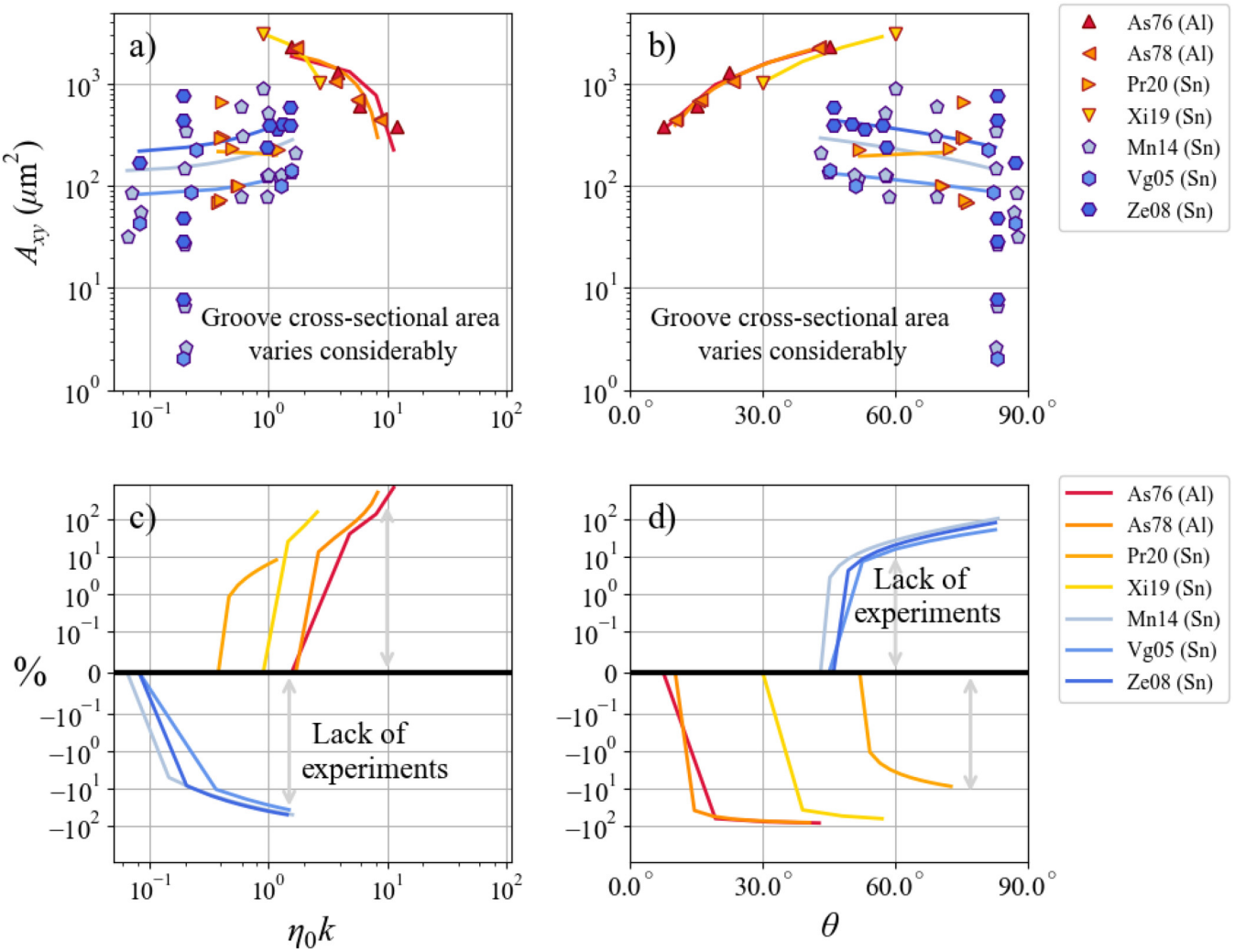

FIG. 7. Previously reported groove cross-sectional areas, A_{xy}, from six investigations as a function of $\eta_0 k$ (a) and θ (b). The solid lines in (a) and (b) represent linear regressions of $A_{xy}(\eta_0 k)$ and $A_{xy}(\theta)$ for each investigation, respectively. (c) and (d) show the percent differences [Eqs. (70) and (71)] between the value of $A_{xy,0}^{-1}$, corresponding to the groove cross-sectional area at the lowest value of $\eta_0 k$ or θ for each regression in (a) and (b), and the values of A_{xy}^{-1} calculated from the rest of the corresponding regressions in (a) and (b). The lines in (c) and (d) indicate jetting factor variations of up to 1000% *due to the variability of groove cross-sectional area alone*, $J_A \sim A_{xy}^{-1}$, holding outflow mass constant.

report the relevant variables for others to directly compare the theories with the experiment data.

The second set of missing experiments is indicated in Fig. 7, where no curve lies within an order of magnitude of the black line representing the enforcement of a constant groove cross-sectional area as θ and $\eta_0 k$ are varied. Groove aspect ratio must be varied *independently* of groove volume to understand the effect of groove aspect ratio on jetting, given that it is reasonably well established that jet mass tends to increase with defect volume,[7,8] holding all else constant. Figure 7 suggests that previous experiments did not vary aspect ratio independently of groove volume. Thus, the jetting factor functions of $\eta_0 k$ and θ implied by Fig. 6 are confounded by groove volume variability. To understand the effect of groove aspect ratio on jetting, sets of groove experiments that are designed to hold groove volume constant [i.e., satisfy Eq. (59)] while varying the groove aspect ratio are necessary. For the sake of reproducibility and direct comparison, future experiments should report groove half angle θ or $\eta_0 k$ accompanied by either groove depth h_0 (or groove amplitude $\eta_0 = h_0/2$) or groove width λ. Reporting θ or $\eta_0 k$ without a depth or width measurement makes it impossible to calculate groove cross-sectional areas [Eqs. (8) and (9)].

ACKNOWLEDGMENTS

This work was supported by the U.S. Department of Energy through the Los Alamos National Laboratory. Los Alamos National Laboratory is operated by Triad National Security, LLC, for the National Nuclear Security Administration of the U.S. Department of Energy (Contract No. 89233218CNA000001).

AUTHOR DECLARATIONS

Conflict of Interest

The authors have no conflicts to disclose.

Author Contributions

B. E. Kaiser: Conceptualization (equal); Data curation (equal); Formal analysis (equal); Investigation (equal); Visualization (equal); Writing – original draft (equal); Writing – review & editing (equal). **I. L. Tregillis:** Conceptualization (equal); Writing – review & editing (equal). **F. J. Cherne:** Conceptualization (equal); Writing – review & editing (equal). **A. C. Koskelo:** Conceptualization (equal); Funding acquisition (equal); Resources (equal); Writing – review & editing (equal).

DATA AVAILABILITY

Data sharing is not applicable to this article as no new data were created or analyzed in this study.

REFERENCES

[1]W. T. Buttler, R. J. Williams, and F. M. Najjar, J. Dyn. Behav. Mater. **3**, 151 (2017).
[2]R. D. Richtmyer, Commun. Pure Appl. Math. **8**, 297 (1960).
[3]E. E. Meshkov, Sov. Fluid Dyn. **4**, 101 (1969).
[4]M. Brouillette, Annu. Rev. Fluid Mech. **34**, 445 (2002).
[5]W. T. Buttler, D. M. Oró, D. L. Preston, K. O. Mikaelian, F. J. Cherne, R. S. Hixson, F. G. Mariam, C. Morris, J. B. Stone, G. Terrones, and D. Tupa, J. Fluid Mech. **703**, 60 (2012).
[6]F. J. Cherne, J. E. Hammerberg, M. J. Andrews, V. Karkhanis, and P. Ramaprabhu, J. Appl. Phys. **118**, 185901 (2015).
[7]J. Xin, A. He, W. Liu, G. Chu, M. Yu, W. Fan, Y. Wu, T. Xi, M. Shui, Y. Zhao, and P. Wang, J. Micromech. Microeng. **29**, 095011 (2019).
[8]J. Asay and L. Bertholf, "Model for estimating the effects of surface roughness on mass ejection from shocked materials," SAND 78-1256, 1978.
[9]E. Buckingham, Phys. Rev. **4**, 345 (1914).
[10]B. R. Munson, T. H. Okiishi, W. W. Huebsch, and A. P. Rothmayer, *Fundamentals of Fluid Mechanics* (Wiley, 2013).
[11]W. S. Vogan, W. W. Anderson, M. Grover, J. E. Hammerberg, N. S. P. King, S. K. Lamoreaux, G. Macrum, K. B. Morley, P. A. Rigg, G. D. Stevens, W. D. Turley, L. R. Veeser, and W. T. Buttler, J. Appl. Phys. **98**, 113508 (2005).
[12]M. B. Zellner, W. V. McNeil, J. E. Hammerberg, R. S. Hixson, A. W. Obst, R. T. Olson, J. R. Payton, P. A. Rigg, N. Routley, G. D. Stevens, W. D. Turley, L. Veeser, and W. T. Buttler, J. Appl. Phys. **103**, 123502 (2008).
[13]J. Asay, "Material ejection from shock-loaded free surfaces of aluminum and lead," Technical Report, 1976.
[14]T. De Rességuier, E. Lescoute, A. Sollier, G. Prudhomme, and P. Mercier, J. Appl. Phys. **115**, 043525 (2014).
[15]K. Mackay, F. Najjar, S. Ali, J. Eggert, T. Haxhimali, B. Morgan, H. Park, Y. Ping, H. Rinderknecht, C. Stan, and A. M. Saunders, J. Appl. Phys. **128**, 215904 (2020).
[16]G. Birkhoff, D. P. MacDougall, E. M. Pugh, and S. G. Taylor, J. Appl. Phys. **19**, 563 (1948).
[17]W. P. Walters and J. A. Zukas, *Fundamentals of Shaped Charges* (John Wiley & Sons, 1989).
[18]L. Soulard, J. Appl. Phys. **133**, 085901 (2023).
[19]M. Xu, W. Song, C. Wang, P. Wang, J. Shao, and E. Tang, Int. J. Impact Eng. **156**, 103944 (2021).
[20]E. M. Pugh, R. Eichelberger, and N. Rostoker, J. Appl. Phys. **23**, 532 (1952).
[21]R. J. Eichelberger, J. Appl. Phys. **26**, 398 (1955).
[22]K. Meyer and P. Blewett, Phys. Fluids **15**, 753 (1972).
[23]G. Dimonte and P. Ramaprabhu, Phys. Fluids **22**, 014104 (2010).
[24]K. O. Mikaelian, Phys. Rev. Lett. **80**, 508 (1998).
[25]Q. Zhang, Phys. Rev. Lett. **81**, 3391 (1998).
[26]A. L. Velikovich and G. Dimonte, Phys. Rev. Lett. **76**, 3112 (1996).
[27]G. I. Taylor, Proc. R. Soc. A Math. Phys. Sci. **201**, 192 (1950).
[28]J. Thouvenin, *Détonique* (Eyrolles, 1997).
[29]Y. Yang, Q. Zhang, and D. H. Sharp, Phys. Fluids **6**, 1856 (1994).
[30]M. Vandenboomgaerde, C. Mügler, and S. Gauthier, Phys. Rev. E **58**, 1874 (1998).
[31]K. O. Mikaelian, Phys. Fluids **6**, 356 (1994).
[32]K. O. Mikaelian, Phys. Rev. E **81**, 016325 (2010).
[33]S. P. Marsh, *LASL Shock Hugoniot Data* (University of California Press, 1980), Vol. 5.
[34]M. Antipov, V. Arinin, A. Georgievskaya, I. Gnutov, D. Zamyslov, D. Kalashnikov, M. Lebedeva, A. Lebedev, A. Mikhailov, V. Ogorodnikov, and K. N. Panov, J. Dyn. Behav. Mater. **3**, 300 (2017).
[35]J. E. Hammerberg, W. T. Buttler, A. Llobet, C. Morris, J. Goett, R. Manzanares, A. Saunders, D. Schmidt, A. Tainter, W. Vogan-McNeil and C. Wilde, "Shock compression of condensed matter—2017," in *AIP Conference Proceedings* (AIP Publishing, 2018), Vol. 1979, pp. 080006-1–080006-5.
[36]W. T. Buttler, R. K. Schulze, J. J. Charonko, J. C. Cooley, J. E. Hammerberg, J. D. Schwarzkopf, D. G. Sheppard, J. J. Goett III, M. Grover, B. M. La Lone, and S. K. Lamoreaux, Physica D **415**, 132787 (2021).
[37]D. B. Bober, K. K. Mackay, M. C. Akin, and F. M. Najjar, J. Appl. Phys. **130**, 045901 (2021).
[38]V. Frachet, P. Elias, J. Martineau, S. Schmidt, and N. Holmes, Shock Waves Condens. Matter **87**, 235 (1988).
[39]D. Hayes, R. Hixson, and R. McQueen, in *AIP Conference Proceedings* (American Institute of Physics, 2000), Vol. 505, pp. 483–488.
[40]B. J. Jensen, F. J. Cherne, M. B. Prime, K. Fezzaa, A. J. Iverson, C. Carlson, J. Yeager, K. J. Ramos, D. E. Hooks, J. C. Cooley, and G. Dimonte, J. Appl. Phys. **118**, 195903 (2015).
[41]A. Mikhailov, V. Ogorodnikov, V. Sasik, V. Raevskii, A. Lebedev, D. Zotov, S. Erunov, M. Syrunin, V. Sadunov, N. Nevmerzhitskii, and S. A. Lobastov, J. Exp. Theor. Phys. **118**, 785 (2014).
[42]S. Monfared, D. Oró, M. Grover, J. Hammerberg, B. LaLone, C. Pack, M. Schauer, G. Stevens, J. Stone, W. Turley, and W. T. Buttler, J. Appl. Phys. **116**, 063504 (2014).
[43]G. Prudhomme, T. De Rességuier, C. Roland, A. Sollier, E. Lescoute, D. Loison, and E. Brambrink, J. Appl. Phys. **128**, 155903 (2020).
[44]D. S. Sorenson, R. W. Minich, J. L. Romero, T. W. Tunnell, and R. M. Malone, J. Appl. Phys. **92**, 5830 (2002).
[45]K. Popper, *The Logic of Scientific Discovery* (Routledge, 1934).